ACS APPLIED MATERIALS & INTERFACES

Article

Multifunctional nickel phosphate nano/micro flakes 3D electrode for electrochemical energy storage, non-enzymatic glucose and sweat pH sensors

Narayanasamy Padmanathan, Han Shao, and Kafil M. Razeeb

ACS Appl. Mater. Interfaces, **Just Accepted Manuscript** • DOI: 10.1021/acsami.7b17187 • Publication Date (Web): 20 Feb 2018

Just Accepted

ACS Publications

ACS Applied Materials & Interfaces is published by the American Chemical Society.
1155 Sixteenth Street N.W., Washington, DC 20036

Multifunctional nickel phosphate nano/micro flakes 3D electrode for electrochemical energy storage, non-enzymatic glucose and sweat pH sensors

N. Padmanathan[1], Han Shao[1,2] and Kafil M. Razeeb[1*]

[1]Micro-Nano Systems Centre, Tyndall National Institute, University College Cork, Dyke Parade, Lee Maltings, Cork T12 R5CP, Ireland

[2]Department of Chemistry, University College Cork, Cork T12 YN60, Ireland

***Corresponding Author**: Dr. Kafil M. Razeeb (kafil.mahmood@tyndall.ie)

Abstract:

Multifunctional, low-cost electrode and catalyst are desirable for next generation electrochemical energy storage and sensor applications. In this study, we demonstrate the fabrication of $Ni_3(PO_4)_2{\cdot}8H_2O$ nano/micro flakes layer on nickel foam (NF) by a facile one-pot hydrothermal approach and investigated this electrode for multiple applications including sweat based glucose and pH sensor as well as hybrid energy storage device, e. g., supercapattery. The electrode displays a specific capacity of 301.8 mAh g^{-1} (1552 F g^{-1}) at an applied current of 5 mA cm^{-2} and able to retain 84% of its initial capacity after 10,000 cycles. Furthermore, the supercapattery composed of $Ni_3(PO_4)_2{\cdot}8H_2O$/NF as positive and activated carbon as negative electrodes can offer a high specific energy of 33.4 Wh kg^{-1} with the power of 165.5 W kg^{-1}. As an electro-catalyst for non-enzymatic glucose sensor, the $Ni_3(PO_4)_2{\cdot}8H_2O$/NF shows an exceptional sensitivity (24.39 $mAmM^{-1}cm^{-2}$) with a low detection limit of 97 nM (S/N=3). Moreover, as a sweat based pH sensor the electrode is capable of detecting human sweat pH values ranging from 4 to 7. Therefore, this 3D nanoporous $Ni_3(PO_4)_2{\cdot}8H_2O$/NF electrode, due to its excellent electrochemical performance can be successfully applied in electrochemical energy storage and biosensor applications.

Keywords: Multifunctional electrode, nickel phosphate, supercapattery, non-enzymatic glucose sensor, sweat pH sensor

Introduction

The enormous propagation of modern electronics industry largely entails the implementation of highly efficient electrochemical devices for wide range of applications. In recent years, the electrochemical devices including supercapacitors, batteries, supercapatteries, and sensors have been realized successfully and demonstrated for the application of portable and bioelectronics devices [1-3]. Most of these devices are integrated together to create an electrochemical device[4-5]. This promotes the necessity of multifunctional materials, which can be used for the fabrication of these different components in a functional device. Therefore, the design of cost-effective electrode or electro-catalyst materials with delicate hierarchical morphology and multiple functionalities has great potential for integrated electrochemical energy storage and sensors. In terms of energy storage, supercapacitor (SC) is one of the clean and eco-friendly renewable energy storage device, which have been used in many of applications[6].Particularly, due to their inherent characteristics such as rapid charge–discharge, high power density and long cycle life, they are highly preferred for portable electronics, electric vehicles, aircrafts, and smart grids[6-7]. Meantime, other electrochemical devices which are powered by energy storage devices such as continuous glucose and pH sensors are also been drawn great importance in medical and food industries[8]. Eventually, integrating these functional device into one will be an ultimate strategy to develop advanced wearable or implantable bio-electronic devices. Numerous active metal/metal oxide nano architectures are being investigated for energy storage and non-enzymatic sensors. Thanks to the transition metal based oxides (i.e. NiO, Co_3O_4, $NiCo_2O_4$, etc.)[9], chalcogenides (MoS_2, NiS, NiTe, etc.)[10] and phosphates ($Mn_3(PO_4)_2$, $Co_3(PO_4)_2$, $Ni_3(PO_4)_2$, etc.)[11], which possess multi-functionalities towards various electrochemical applications. Among them, metal phosphates are being studied for electrochemical energy storage[11]. Yang et al. proposed manganese (II) phosphate nanosheets with graphene for all solid state supercapacitor[12]. Unique layered $NH_4CoPO_4{\cdot}H_2O$ micro-

bundles has been reported for supercapacitor application[13], while $Ni_3P_2O_8$ and $Co_3P_2O_8{\cdot}8H_2O$ based composite was investigated as positive electrode for asymmetric supercapacitors[14].

In case of electrode for energy storage devices (i.e. supercapacitors), it should be noted that not all the redox or Faradaic processes may contribute directly to capacitive current and voltage characteristics, since fuel cell mechanism and electroplating also faradaic in nature but differ from capacitor. Therefore, such a non-capacitive Faradaic charge storage process should be excluded from discussions on pseudo-capacitive Faradaic processes. Hence, these kinds of non-capacitive energy storage processes are categorized under supercapattery, which showed distinct non-capacitive or battery like charge-discharge characteristic[15]. In addition to energy storage, these materials exhibit superior catalytic activity towards electrochemical pH and glucose sensors with some distinct advantages such as high sensitivity, simple operation, excellent accuracy, and inexpensive platform[16-17]. Till date, there is a wide range of solid state and oxide based pH and glucose sensor available in the research domain[17-22]. The commonly used sensor probe is sensitive, stable and lasts for a relatively long period of time but it is not a practical sensor for pH or glucose measurements in all environments, particularly in wearable ambulatory settings[19]. The determination of pH/glucose on external skin or from sweat with conventional sensor is much difficult in terms of applicability. For this measurement, different metal oxide nanostructures IrO_2, $Ni(OH)_2$, CuO, ZnO, etc., also been proposed[18, 20-22]. However, they are sensitive to redox reagents and temperature, which depends on the metal. Stability, repeatability and bio-fouling are the eminent issues in these electrodes, which are yet to be resolved. Thereby, there is no multi-analyte sensor available that can measure both pH and/or glucose from sweat in commercial domain. Hence, in this work we focus for the development of novel multifunctional electrode materials with high electrochemical activity towards different electrochemical applications of supercapattery, non-enzymatic glucose and pH sensors.

The most common requirements for the appropriate electrode/catalyst materials include good surface wettability, high sensitivity and long term stability. Metal phosphates owing to their excellent electrochemical properties have received good attention for the development of supercapattery and biosensors. Among various metal phosphates, transition metal phosphates such as Ni/Co based phosphates structures have been widely investigated for electrochemical applications[11, 23-24]. Here, Ni or Co play a significant role in the electrochemical activity while P influence to form a stable structure[24]. Pang et al. initially proposed $NH_4CoPO_4{\cdot}H_2O$ nano/microstructures as a high performance electrode material for electrochemical energy storage devices[25]. In continuation, a significant number of efforts have been made to use other metal phosphate as the electrode for energy storage devices[11]. Our previous report concluded that direct integration of $Co_3(PO_4)_2{\cdot}8H_2O$ multilayer nano/micro flakes on nickel foam can be a superior electrode for supercapatteries[26]. In practice, it has been reported that cobalt based materials have been prone to transform into amorphous Co-Pi or cobalt oxide phases during redox process[27-28]. Also, Co based catalyst are usually regarded as a less abundant toxic material, and using as sensor catalyst would cause further discrepancies and should be replaced with suitable alternatives[29]. Therefore, focus have been devoted to Ni based electro-catalyst materials, which possess similar electrochemical activity like Co and more abundant in nature. Ammonium intercalated nickel phosphate hydrate nanostructure has been proposed for supercapacitor[30]. Similarly, three dimensional Ni_2P nanoarray has been developed as an efficient catalyst electrode for sensitive and selective non-enzymatic glucose sensor[31]. Recently, nanoporous nickel phosphate (i.e. $Ni_{20}[(OH)_{12}(H_2O)_6][(HPO_4)_8(PO_4)_4]{\cdot}12H_2O$) VSB 5 (Versailles Santa Barbara-5) nanorod carbon paste electrode based glucose sensor has been reported[32]. However, the poor electrochemical sensing performance, and low specific capacity limited their further development to practical applications. Noticeably, the electrochemical activity of crystalline $Ni_3(PO_4)_2{\cdot}8H_2O$ based electrode materials are

rarely been investigated. To the best of our best knowledge, there is no report of $Ni_3(PO_4)_2 \cdot 8H_2O$ either for glucose or pH sensors.

Herein, we describe a facile route to fabricate $Ni_3(PO_4)_2 \cdot 8H_2O$ nano/micro flakes structure on NF via one-pot hydrothermal technique without any additives or templates. This 3D nano/microstructure is investigated as a binder-free electrode for supercapattery and highly sensitive catalyst for non-enzymatic glucose and pH sensor in sweat. When applied as a positive electrode for supercapattery, $Ni_3(PO_4)_2 \cdot 8H_2O$/NF based device delivers a maximum specific capacity of 67.4 mAh g^{-1} at a specific current of 2.5 mA cm^{-2} with 89% retention capability after 10,000 cycles. It can achieve a high specific energy of 33.4 Wh kg^{-1} and power of 165.5 W kg^{-1}, demonstrating impressive energy storage performance. As a non-enzymatic glucose sensor, the electrode exhibit higher sensitivity than state of the art non-enzymatic glucose sensor with a detection limit of 97 nM. Moreover, $Ni_3(PO_4)_2 \cdot 8H_2O$ nano/micro flakes has been tested as a potentiometric sweat based pH sensor, which showed a high pH response for general human sweat pH ranges of 4 - 7 with good selectivity.

Experimental Procedures

Analytical grades of Nickel chloride hexahydrate ($NiCl_2 \cdot 6H_2O$), Ammonium dihydrogen phosphate ($NH_4H_2PO_4$) and polyethylene glycol (PEG) were purchased from Sigma Aldrich, and used as received without further purifications. For typical synthesis, 10 mM of $NH_4H_2PO_4$ was first dissolved in 80 ml of deionized water followed by the addition of equal mole of $NiCl_2 \cdot 6H_2O$ to the above solution under vigorous stirring at room temperature. Subsequently, 5 ml of PEG was added into the above mixture to form a homogeneous solution. After stirring for 20 min, the solution was transferred to reaction vessel of volume 100 ml, which contains pretreated NF (3×3 cm^2) and kept at 120 °C for 4 h. Finally, after cooling down to room temperature, the $Ni_3(PO_4)_2 \cdot 8H_2O$ grown NF was take off and washed 3 times using deionized water, Ethanol and Acetone, and dried in an oven at 120 °C for 12 h. The mass loading on NF

was carefully estimated from the mass difference before and after $Ni_3(PO_4)_2 \cdot 8H_2O$ growth using a PioneerTM (PA214C), USA with 0.00001 g reliability and found to be ~2.4 mg cm^{-2}.

Material Characterizations

The phase analysis of the sample was performed by X-ray diffraction (XRD) using a Philips PW3710-MPD diffractometer with Cu Kα radiation (λ = 1.5418 Å). Renishaw (RA 100) inVia confocal Raman Microscope with 514.5 nm excitation laser wavelength was used to observe the Raman spectra of the sample. The Fourier Transform Infrared (FTIR) spectrum was recorded using a Perkin-Elmer Spectrum Two FTIR spectrophotometer. The morphology and composition of the as-prepared sample was observed by a FEI QUANTA 650 field-emission scanning electron microscope (FE-SEM) with an energy dispersive X-ray spectroscopy (EDX Oxford Instruments INCA energy system) at an acceleration voltage of 20.0 kV. High resolution Transmission microscope (JEOL HRTEM-2100 at 200 kV) was used to understand the internal microstructure of the material. To avoid the Ni contribution from the NF substrate, the EDX and TEM measurements were carried out for the powder samples scratched off from the NF. The X-ray photoelectron spectroscopy (XPS) analysis was performed on a Kratos Ultra DLD spectrometer with Al K α (1486.6 eV) as the X-ray source. Nitrogen adsorption–desorption measurements were performed in a Gemini VII 2390 Analyzer at 77 K using the volumetric method. The specific surface area was obtained from the N_2 adsorption–desorption isotherms and was calculated by the Brunauer–Emmett–Teller (BET) method.

Electrochemical measurement of supercapattery

All the electrochemical characterizations were carried out using a CHI 660C electrochemical workstation and a Bio-logic VSP Modular 5 channels potentiostat. Binder free $Ni_3(PO_4)_2 \cdot 8H_2O$ on NF, platinum wire and saturated calomel electrode were used as working, counter and reference electrodes, respectively.

1 M sodium hydroxide solution (NaOH) was used as the supporting electrolyte. The activated carbon electrode was prepared by spreading the mixture of activated carbon (85 wt%), and PVDF (polyvinylidene difluoride) (15 wt%) on nickel foam. The mass loading of the negative electrode (m_-) can be determined using the relation: $\frac{m_+}{m_-} = \frac{C_- \times \Delta E_-}{C_+ \times \Delta E_+}$, where m_+ is the mass loading of the positive electrode, C_- and C_+ are the specific capacitance and specific capacity of the negative and positive electrodes and ΔE_- and ΔE_+ are the corresponding potential limit, respectively. Typical mass loading of AC/NF electrode was ~5.1 mg cm^{-2}. The electrochemical performance of the supercapattery was evaluated by cyclic voltammetry, charge-discharge studies and electrochemical impedance spectra analysis (EIS).

Electrochemical studies of Glucose and pH sensors

The as-prepared $Ni_3(PO_4)_2 \cdot 8H_2O$/NF electrode was applied for the development of non-enzymatic glucose and pH sensor. The electrochemical performance of the sensor was tested in a three electrode system with the $Ni_3(PO_4)_2 \cdot 8H_2O$/NF, Pt and Ag/AgCl as working, counter and reference electrodes, respectively. The electrocatalytic activity of bare NF and $Ni_3(PO_4)_2 \cdot 8H_2O$/NF electrodes were recorded in a solution containing 1 M NaOH at a scan rate of 10 mV s^{-1} in the absence and presence of glucose using cyclic voltammetry. The amperometric measurements were carried out in a 1 M NaOH solution with the successive addition of glucose solutions of different concentrations (50 and 100 µM) at an applied potential of 0.45 V vs. Ag/AgCl. The electrode was evaluated as a potentiometric pH sensor by characterizing it's catalytic activity in Britton-Robinson (B-R) Buffer solutions of various pH (2-8) and in standard stimulated sweats of pH 5.5, 6.5 and 8 (obtained from SYNTHETIC URINE e. K. D-71735 Eberdingen-Nußdorf, Germany), using open circuit potential (OCP) measurements in a typical three-electrode setup with platinum wire as counter and Ag/AgCl as reference electrodes. To vary the pH from 2 to 8, 0.2 M NaOH solution was used and monitored using a standard pH meter with ±0.02 resolution.

Results and Discussion

The XRD pattern of the $Ni_3(PO_4)_2{\cdot}8H_2O$/NF is illustrated in Fig. 1(a). The strong peak at 44° and 51° of 2θ is due to pure NF substrate. The intense diffraction peaks located at 14.3°, 18.5°, 29.1°, 31.2°, and 34.5° correspond to the hydrated nickel phosphate phase (JCPDS No. 33-951). There is no peaks from other phosphides or phosphates, confirming a single monoclinic phase of $Ni_3(PO_4)_2{\cdot}8H_2O$ with I_2/m space group is successfully grown over the 3D NF [33]. The intense and narrow diffraction peaks demonstrates high crystallinity of the material. The average crystallite size of $Ni_3(PO_4)_2{\cdot}8H_2O$ flakes was estimated from the Debye-Scherrer equation, $D = \frac{K\lambda}{\beta \cos\theta}$, Where D is the mean size of crystallites (nm), K is crystallite shape factor (a good approximation is 0.9), λ is the X-ray wavelength (λ = 1.5406 Å), β is the full width at half the maximum (FWHM) in radians of the X-ray diffraction peak and θ is the Braggs' angle (degree). The calculated D value for (0 2 0) plane is found to be ~35 nm.

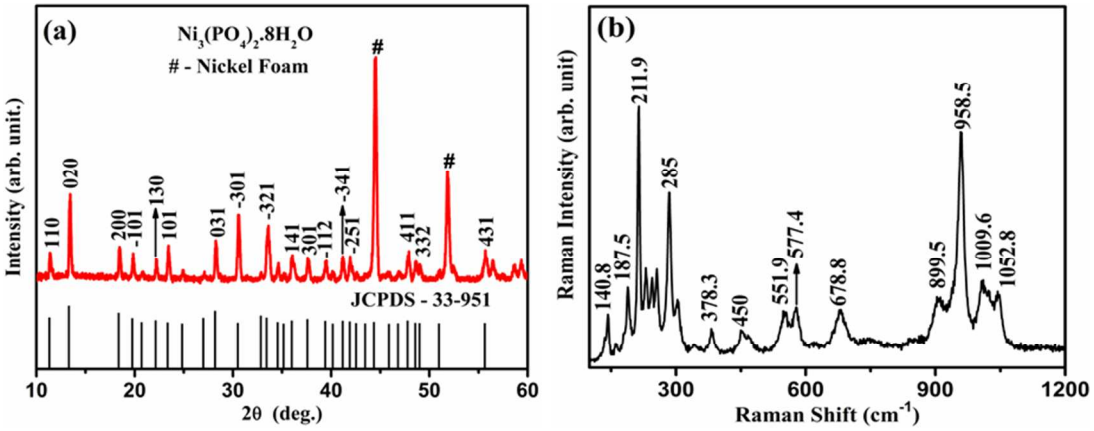

Figure 1. (a) XRD and (b) Raman spectra of $Ni_3(PO_4)_2{\cdot}8H_2O$/NF nano/micro flakes.

Typical Raman spectra in Fig. 1(b) consists of three ranges of vibrations including 140 – 300, 350 – 700 and 900 – 1100 cm^{-1} [26, 34-39]. Raman shifts at 958.5 and 1052.8 cm^{-1} are assigned to the respective ν_1 PO_4^{3-} symmetric and ν_3 PO_4^{3-} antisymmetric stretching modes. There is also a band at 1009.6 cm^{-1} corresponds

to the NiOH deformations modes. A low intensity band at 899.5 cm^{-1} can be a water liberation mode as reported by Breitinger et al. [36]. Raman shift at 678.8 cm^{-1} (within the 350 to 700 cm^{-1} range) is assigned to the v_4 bending modes of PO_4^{3-} unit [38]. Other peaks at 378.5 and 577.4 cm^{-1} indicate the deformation modes of PO_4 and P-O-P, respectively [37]. The corresponding O-P-O bending modes is observed at 450 cm^{-1}. At the low wavenumber region, Raman band at 211.9 and 285 cm^{-1} can be assigned for P-O-P (bridge) bending and M-O stretching (i.e. Ni-O and O-Ni-O) vibrations, respectively. As the metal oxygen stretching occurs in the P-O-P bending region, it is difficult to assign this vibration unambiguously [39]. Also it can be seen that the Raman shifts at 140.8 and 187.5 cm^{-1} are due to external vibrations [34-35]. All these Raman modes are consistent with the observed FTIR spectra shown in Fig. S1 of the Supporting Information (SI). The peaks in the range of 500 - 1000 cm^{-1} belongs to the Ni-O and Ni-P stretching vibrations. The bands at 536.5 and 951 cm^{-1} in the FTIR curve can be assigned to the v_4 (PO_4) and v_1 (PO_4) symmetric stretching vibrations, respectively [35]. The Ni-OH-Ni stretching peak is positioned at 870 cm^{-1} [35]. In addition, the wide band at 2980.3 cm^{-1} and 3441 cm^{-1} in the FTIR curve can be assigned to the v_1 (A1) H_2O and v_3 (B_2) H_2O bond vibrations from the hydrated materials. The corresponding bending mode also being observed at 1600 cm^{-1} [33]. The band with less intensity at 722.3 cm^{-1} is assigned to liberation modes of water molecules. These results further confirms the growth of single phase $Ni_3(PO_4)_2 \cdot 8H_2O$ monoclinic structure over NF support, without any secondary phases.

The surface morphology and microstructure of the nickel phosphate hydrate was analyzed with electron microscope. The SEM images of the $Ni_3(PO_4)_2 \cdot 8H_2O$/NF captured at different magnifications are shown in Fig. 2(a-b). Low magnification SEM image confirms 3D growth of $Ni_3(PO_4)_2 \cdot 8H_2O$/NF nano/micro flakes layers radiating around all the directions. Each layer is randomly assembled and forming the multilayer structure. High magnification SEM image (b) shows interconnected 2D micro flakes, where the average length and thickness of the flakes vary from 5-10 µm and 100-200 nm, respectively. HR-TEM image in Fig. 2(c) confirms the interconnected disordered layer structure.

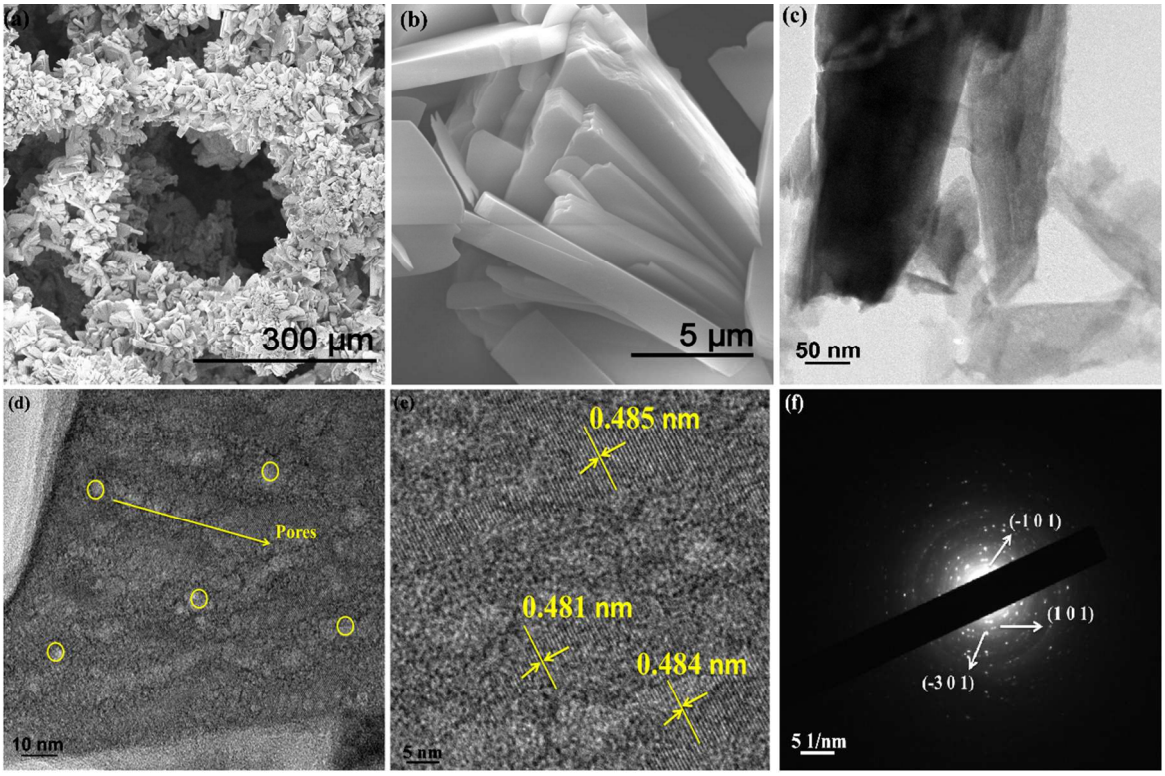

Figure 2. (a-b) SEM images of $Ni_3(PO_4)_2{\cdot}8H_2O$/NF captured at different magnifications, (c) HRTEM image of $Ni_3(PO_4)_2{\cdot}8H_2O$ nano/micro flakes, (d) Individual flake consists of pores, (e) Measured lattice space in layered flakes, and (f) the corresponding SAED pattern.

Further TEM analysis (Fig. 2d) shows visible pores with an average size of 4 nm, reveals mesoporous microstructure of the materials. A well-resolved lattice fringe of ~0.48 nm as shown in Fig. 2(e) can be assigned to (2 0 0) plane of monoclinic $Ni_3(PO_4)_2{\cdot}8H_2O$ crystal structure (JCPDS No. 33-951). The selected area electron diffraction pattern in Fig. 2(f) elucidate polycrystalline nature of the composite, whereas energy dispersive spectroscopy (EDS) analysis in Fig. S2 of the SI reveals the existence of primary Ni, P, and O elements with composition (Fig. S2 inset), asserting successful growth of nickel phosphate without impurities. To further investigate the surface area and pore distribution, N_2 absorption and desorption measurements were carried out, where the corresponding isotherm and pore size distribution curve are shown in Fig. S3 and its inset. According to the IUPAC classification, the type IV

isotherm and BJH-plot was observed for $Ni_3(PO_4)_2 \cdot 8H_2O$ nano/micro flakes and indicating the presence of mesopores on the surface. The BET surface area of the $Ni_3(PO_4)_2 \cdot 8H_2O$ is about 29.8 $m^2\ g^{-1}$ with an average pore diameter of 3.5 nm, which corroborates the TEM observation and confirm ultrafine mesoporous structure of the 3D nano/micro flakes.

X-ray photoelectron spectroscopy was carried out to investigate the atomic valence state of the nickel phosphate multilayer nano/micro flakes. From the XPS survey spectrum in Fig. 3(a), it has been perceived that the primary elements of Ni, P and O are present in the material, which is consistent with the EDS analysis. XPS spectra of Ni 2p, P 2p and O 1s of the sample are shown in Fig. 3(b-c). As seen from Fig. 3(b), Ni 2p consists of two peaks with their respective satellite peaks. The peaks centered at 856.2 and 873.9 eV correspond to the $2p_{3/2}$ and $2p_{1/2}$ splitting of Ni^{2+}, which possibly interacting with the phosphate and hydroxide ions[40-41]. Besides, the presence of two additional deconvoluted peaks at higher binding energies of 858.1 and 875.9 eV in the Ni2p XPS spectra can be assigned to the core levels of Ni^{3+} cations, which indicates the presence of Ni-$(OH)_2$ in the $Ni_3(PO_4)_2 \cdot 8H_2O$ structure[42-43]. In addition, the satellite peaks at 862.2 and 880.2 eV further reveals the existence of Ni at their +2 state. The corresponding P 2p spectra in (c) shows the major peak at 133.1 eV and can be assigned to P-O interactions in nickel phosphate[44]. This XPS results is further supported with O 1s spectra shown in Fig. 3(d). The strong and intense peak at 531.2 eV is associated to the Ni-O and P-O bonding. The small intensity peak positioned at 532.8 eV mainly arises from the hydrates and moisture[45].

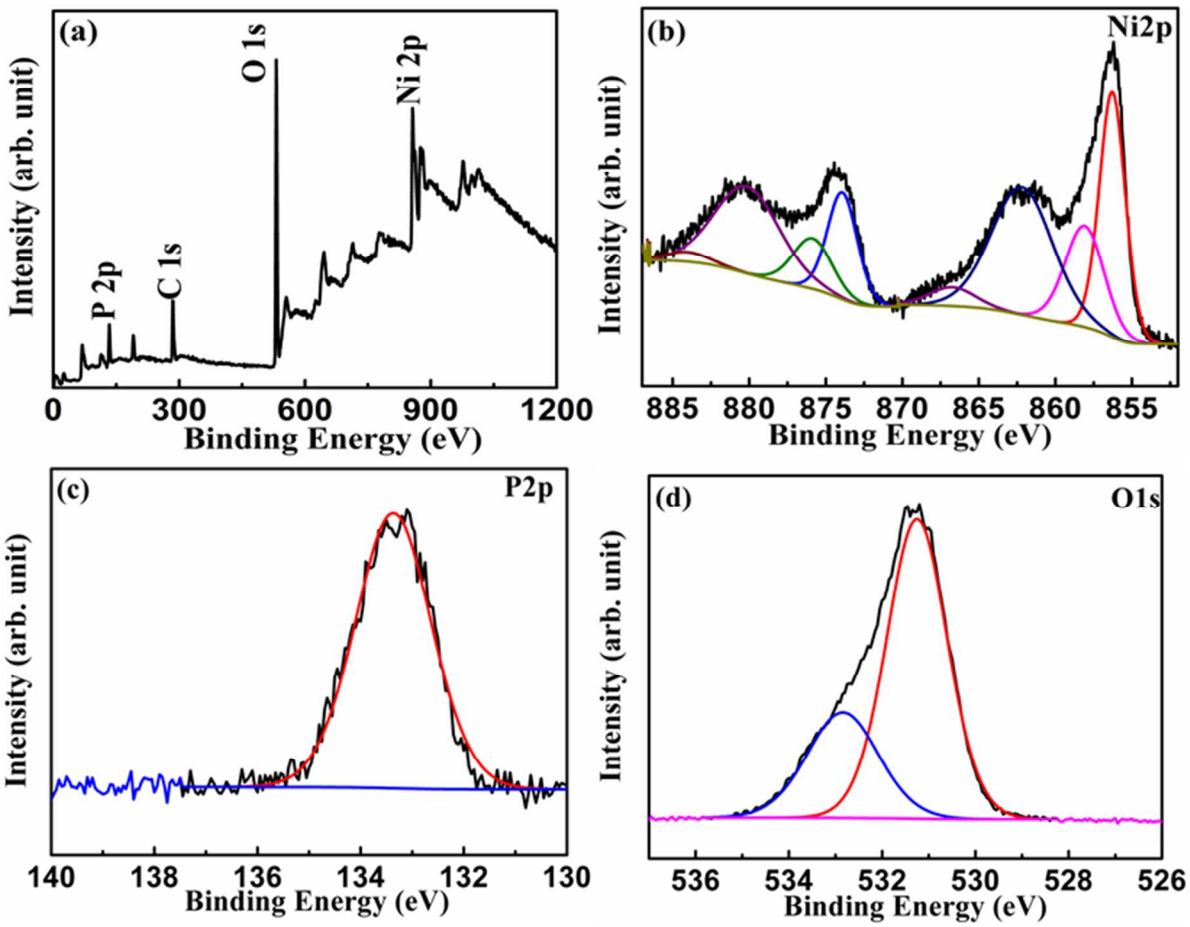

Figure 3. (a-d) XPS survey and core level XPS spectra of nickel phosphate multilayer nano/micro flakes.

Energy Storage studies

In order to explore the potential application as a supercapattery electrode, the $Ni_3(PO_4)_2{\cdot}8H_2O$/NF was examined with cyclic voltammetry, galvanostatic charge-discharge, cyclic stability and electrochemical impedance spectroscopy (EIS) measurements in a three electrode configuration. Fig. 4(a) shows the cyclic voltammogram (CV) at different scan rates ranging from 2-100 mVs^{-1}. The CV curves are different from the ideal supercapacitor suggesting that energy storage mechanism is non-capacitive in nature, which is due to the faradaic pseudo-battery property of the $Ni_3(PO_4)_2{\cdot}8H_2O$/NF nano/micro flakes layers related to the Ni^{2+}/Ni^{3+} redox mechanism[46]. The pairs of the redox peaks are attributed to the oxidation

of nickel phosphate and the reverse reduction processes as suggested by the following chemical reactions (1-3) [26, 47]:

$$Ni_3(PO_4)_2{\cdot}8H_2O + 3OH^- \leftrightarrow Ni_3(PO_4)_2(OH^*)_3{\cdot}8H_2O + 3e^- \quad (1)$$

$$Ni_3(PO_4)_2(OH^*) + OH^- \leftrightarrow Ni_3(PO_4)_2(O^*) + H_2O + e^- \quad (2)$$

$$O^* + O^* \leftrightarrow O_2\uparrow \quad (3)$$

According to Michael et al.[47] the adsorption of OH and O species on the surface lead to the oxygen evolution during electrochemical reaction in alkaline conditions. Since phosphate is not involved to the redox process, during electrochemical reaction there is an adsorption of OH^- ions on the electrode [i. e., $Ni(OH)_2$] surface leads to the oxidation of existing Ni^{3+} to Ni^{4+} and allows the formation of OH* followed by the O* and thus results the oxygen evolution at the end[47-48]. The high current response in the CV curves is mainly due to the contribution of more active sites from the $Ni_3(PO_4)_2{\cdot}8H_2O$ layers and implies the excellent charge storage capacity of the electrode. As the scan rate increases, the peak current increases and the redox potential start to shift more positive and negative regions, indicating quasi-reversibility of the electrode.

The charge-discharge (CD) studies under different specific current further supports the electrochemical response, observed from the CV analysis. The CD curve with distinct plateaus as shown in Fig. 4(b) confirms the Faradaic pseudo-battery type energy storage with quasi-reversibility of the $Ni_3(PO_4)_2{\cdot}8H_2O$ nano/micro flakes layered electrode. Since the observed energy storage phenomenon is non-capacitive, the average charge storage capacity and capacitance at the electrode surface was calculated using the following relations as reported earlier:[40, 49]

Specific capacity (mAh g^{-1}) of electrode material in a three electrodes system

$$C = \frac{I \times t}{3.6m} \quad (4)$$

where, *I* is the charge-discharge current (mA), *t* is the discharge time (s), *m* is the mass loading of active material (mg).

Specific capacitance (F g^{-1}) of electrode material in a three electrodes system

$$C = \frac{I \times t}{m \times V} \quad (5)$$

where, *I* is the charge-discharge current (mA), *t* is the discharge time (s), *m* is the mass loading of active material (mg) and *V* is the active potential regime (V).

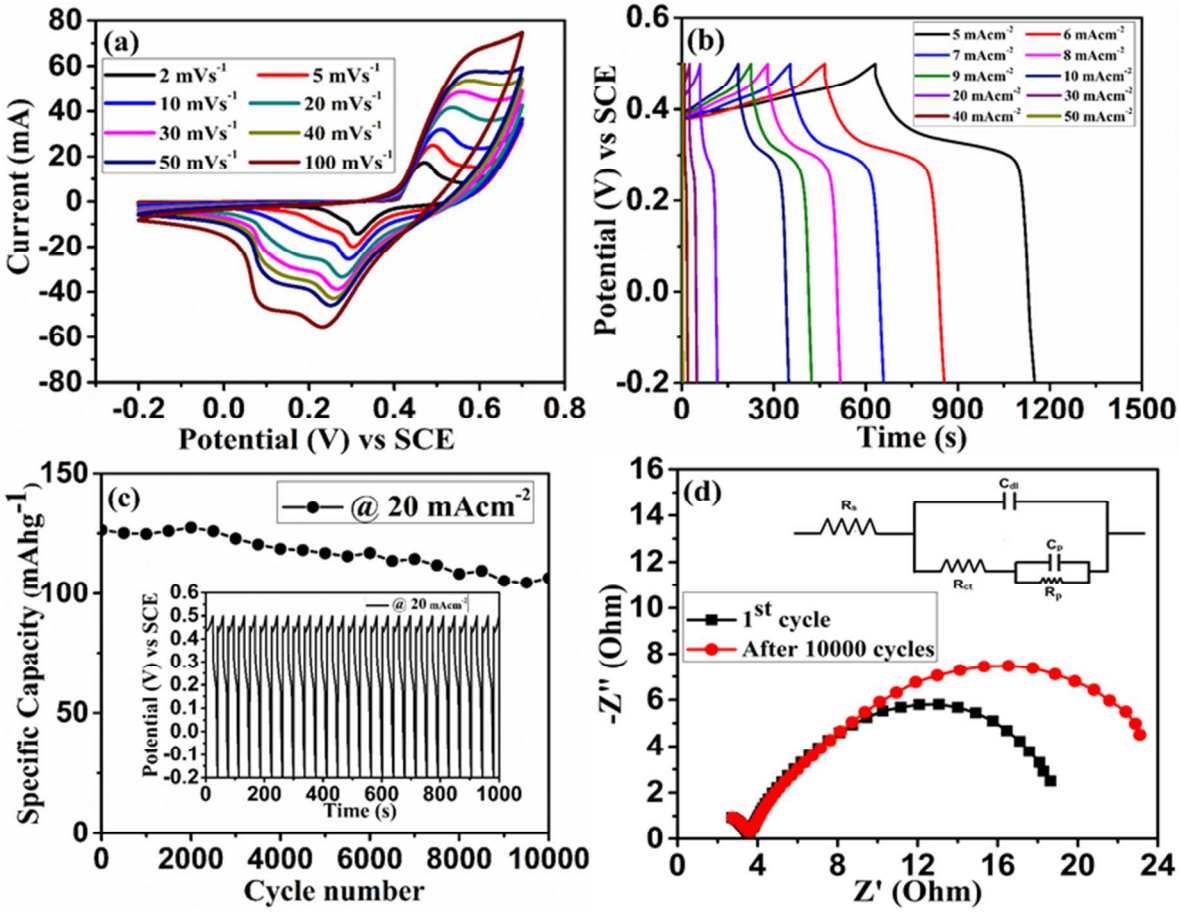

Figure 4. (a) Cyclic voltammogram of $Ni_3(PO_4)_2 \cdot 8H_2O$ nano/micro flakes electrode at different scan rates of 2 – 100 mV s^{-1}, (b) Charge-discharge profile at various applied current of 5 – 50 mA cm^{-2}, (c) Cyclic stability of the electrode at 20 mA cm^{-2} and inset represents the continuous charge discharge curve, (d) Nyquist plot of the electrode before and after 10,000 charge-discharge cycles and the corresponding equivalent circuit (inset).

The measured specific capacity of the electrode was found to be 301.8 mAh g^{-1} (1552.3 F g^{-1}), 270.4 mAh g^{-1} (1390.8 F g^{-1}), 246.9 mAh g^{-1} (1270.1 F g^{-1}), 220.2 mAh g^{-1} (1132.4 F g^{-1}), 203.8 mAh g^{-1} (1048.3 F g^{-1}) and 189.5 mAh g^{-1} (974.7 F g^{-1}) for 5, 6, 7, 8, 9 and 10 mA cm^{-2} respectively. Recently, Chen et al. showed a specific capacitance of 964 F g^{-1} at 5 A g^{-1} for NH_4 intercalated $Ni_3(PO_4)_2{\cdot}H_2O$@NF.[50] Similarly, layered $NH_4Co_xNi_{1-x}PO_4{\cdot}H_2O$ nanostructures exhibit specific capacitance of 1567 and 1212 F g^{-1} at 1 A g^{-1} with and without Co.[51] In earlier, Zhao et al. showed a capacitance of 1497 F g^{-1} at 1.25 A g^{-1} for $Ni_{20}[(OH)_{12}(H_2O)_6][(HPO_4)_8(PO_4)_4]{\cdot}12H_2O$ nanorods[52]. It is worth mentioning that all these reports are for mostly intercalated metal phosphates or pyrophosphates and $Ni_3(PO_4)_2{\cdot}8H_2O$ is rarely been reported. Thereby with such a high energy storage capacity (e.g., 1552.3 F g^{-1} at 5 mA cm^{-2}), our $Ni_3(PO_4)_2{\cdot}8H_2O$ based electrode is superior to other nickel phosphate and metal phosphate based electrodes reported so far.

The cyclic stability of the electrode was evaluated by continuous charge-discharge measurements at 20 mA cm^{-2} (Fig. 4c). The proposed nickel phosphate nano/micro flake layered structure possesses excellent cyclic stability with 84% retention capacity even after 10,000 cycles. Typical reaction kinetics of the electrode was further interrogated by an electrochemical impedance spectroscopy (EIS) and presented in a Nyquist plot in Fig. 4(d). These spectra show typical two-time-constants behavior: one appearing as large semicircle in the low frequency region and other as an incomplete semicircle at high frequency. Noticeably, the impedance which is related to charge transfer at the electrode surface is quite similar for before and after cycling, demonstrating consistent electrical conductivity of the electrode. An increment in the high frequency semicircle after 10,000 cycles reveals the adsorption of reaction intermediates. The existence of these two characteristic processes are associated with the adsorption/desorption of intermediates and the diffusion controlled Faradaic reactions (electron/ion transfer) at the electrode/electrolyte interface. The observed Nyquist plot was fitted with an equivalent circuit as described by Ho et al.[53] and shown in the inset of Fig. 4(d). Here the R_s, R_{ct} and C_{dl}, represents the

solution resistance, charge transfer resistance and double layer capacitance.[40] The elements C_p and R_p are associated with adsorption and desorption of reaction intermediates as quoted in electrochemical reactions (1-3).[53] These reactions are commonly interpreted in terms of Faradaic reaction in the presence of adsorption of the reaction intermediates (i.e. $OH^{\bullet}$ radical). The occurrence of the two depressed semicircles in the complex-plane plot in the presence of Faradaic reactions is not well-understood for real porous electrode and need more investigations. However, it can be seen that the time constant associated with the adsorption of intermediates is large compared to that of the charge transfer kinetics and hence the low frequency semicircle is typically associated with the adsorption process whereas the high frequency semicircle is associated with the redox kinetics.[53]

Considering the high performance of the $Ni_3(PO_4)_2{\cdot}8H_2O$ micro/nano flakes electrode at three electrode configuration, several hybrid supercapatteries were fabricated with $Ni_3(PO_4)_2{\cdot}8H_2O$/NF (NP/NF) as the positive and activated carbon/NF (AC/NF) as the negative electrodes. The different operating voltages of the NP (-0.2 to +0.5 V) and AC (−1 to 0 V) indicate a good match in the potential windows for an asymmetric supercapattery (Fig. S4). Fig. 5(a-d) summarizes the performance of our hybrid supercapattery in 1 M NaOH electrolyte. The CV curves (Fig. 5a) retaining their battery like characteristic even at a high scan rate of 100 mVs^{-1} indicate excellent rate capacity of the device. Fig. 5(b) shows the charge-discharge profile of the $Ni_3(PO_4)_2{\cdot}8H_2O$/NF ||AC/NF hybrid supercapattery at various specific current ranging from 2.5 to 20 $mAcm^{-2}$. The specific capacity of the device was calculated from the discharge curve based on the active material masses of the device (~7.5 mg cm^{-2}) using equation (4). The specific capacities are 67.4, 58.9, 52.3, 52.7, 46.3, 41.7, 26.8 and 16 mAh g^{-1} for 2.5, 3, 3.5, 4, 4.5, 5, 10 and 20 mA cm^{-2}, respectively. In addition, the supercapattery showed excellent cyclic stability of up to 10,000 cycles as shown in Fig. 5(c) and retained 89% of initial capacity at 20 $mAcm^{-2}$. The coulombic efficiency of the device was found to be 96.5% for the first few cycles and reached to ~99%, and was quite stable up to 10,000 cycles (Fig. 5c), indicating steady redox process at the electrode surface.

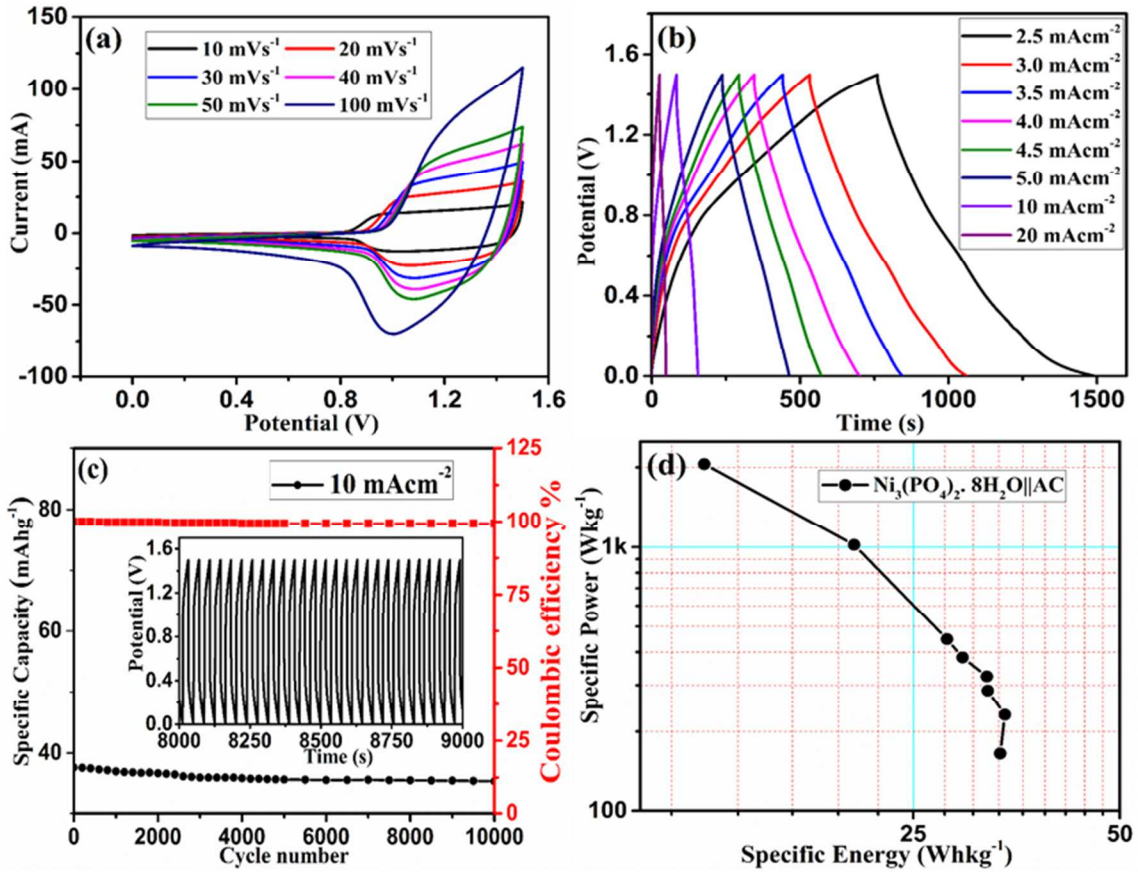

Figure 5. (a) Cyclic voltammogram of $Ni_3(PO_4)_2 \cdot 8H_2O$/NF ‖ AC/NF supercapattery at different scan rates of 10 – 100 mVs^{-1}, (b) Charge-discharge profile for the device at different specific current of 2.5 – 20 mA cm^{-2}, (c) Cyclic stability and coulombic efficiency of the device at 10 mA cm^{-2} and inset represents the corresponding charge discharge profile, (d) Ragone plot related to the specific energy and power of the device.

Since the electrode kinetics are non-capacitive, the specific energy and power of the device were calculated according to: $E = I \int_{t=0}^{t=t} V(t)dt$ and $P = E/t$ where, *E* is the specific energy (Wh kg^{-1}) based on total active material mass of the electrodes, *P* is the specific power (W kg^{-1}), *I* is the specific current (A g^{-1}) [I = current density (mA cm^{-2})/mass density (mg cm^{-2})], *V* is the potential (V) and *t* is the discharge time (h). Ragone plot for the hybrid cell at different currents are shown in Fig. 5(d). At 2.5 mA cm^{-2} current, our supercapattery delivers a specific energy of 33.5 $Whkg^{-1}$ with a specific power of 165.5 W

kg^{-1}. At a high current of 20 $mAcm^{-2}$, the specific energy and power values are 16 Wh kg^{-1} and 2058.7 W kg^{-1}, respectively. The observed specific energy and power output of the device is quite comparable with the value (35.3 Wh kg^{-1} and 101 W kg^{-1}) reported by Zhao et al. for $(Ni, Co)_3(PO_4)_2 \cdot 8H_2O$[24] and nearly equal to the nickel-cobalt pyrophosphates based asymmetric cell (33.4 Wh kg^{-1} and 399 W kg^{-1})[14]. Interestingly, our supercapattery shows comparable and in some cases better properties than other reported works for similar materials (Table S1 of the Supplementary Information). The Nyquist plots for the supercapattery before and after 10,000 charge- discharge cycles are shown in Fig. S5. The electrical conductivity of the electrode is quite good for the hybrid device and the equivalent series resistance is 0.78 Ω and 5.25 Ω before and after 10,000 cycles. The observed low ESR values confirm the high conductivity and excellent electrical contact between the active material and current collector. From this study it can be concluded that $Ni_3(PO_4)_2 \cdot 8H_2O$ micro/nano flakes could be an excellent candidate as positive electrode for future energy storage devices.

Non-enzymatic glucose sensor analysis

Continuous Glucose Monitoring (CGM) systems have recently been launched in the market, which test interstitial fluid for glucose levels every few minutes[54]. This is very useful as it allows real-time examination of how the blood glucose level varies to insulin, exercise, food, and other factors for diabetic patients[55]. Despite their availability as commercial enzymatic glucose sensor, issues such as cost, poor reproducibility and susceptibility to enzyme poisoning molecules prohibit its widespread use[17]. These problems prompted the development of non-enzymatic glucose sensor for continuous glucose monitoring[54]. Here, for the first time $Ni_3(PO_4)_2 \cdot 8H_2O$ nano/micro flakes directly grown on NF is proposed for non-enzymatic glucose sensor. The CVs of Fig. S6 in the SI shows the redox peaks in the absence and presence of 500 µM glucose for pure nickel foam (NF) and $Ni_3(PO_4)_2 \cdot 8H_2O$/NF. The NF has insignificant electro-catalytic activity when compared to the $Ni_3(PO_4)_2 \cdot 8H_2O$/NF catalyst toward the direct oxidation of glucose. Fig. S7(a) shows the cyclic voltammograms recorded from -0.2 to 0.7 V for

nickel phosphate electrode at several scan rates in 1 M NaOH with 500 µM glucose. Both anodic and cathodic peak current increases with the scan rates. The observed linear relationship of the current densities and square root of the scan rates in Fig. S7(b) implies dominant diffusion controlled glucose oxidation process rather than surface-controlled reaction[32]. This results was further validated by the observed non-linearity between current density (J_{pa}) vs. scan rate (ν) plot as shown in Fig. S8(a). In addition, the plot of log I_{pa} vs. log ν (Fig. S8b) shows the typical slope value of 0.39, which is less than the predicted value of (0.5) pure diffusion controlled process. This infers kinetics limitation in the overall reaction[56]. To date there is no exact mechanism for glucose oxidation on Ni based electrodes in alkaline medium. The accepted mechanism of oxidation of glucose to gluconolactone by the well-known Ni^{3+}/Ni^{2+} redox couples can be shown as follows:[57]

$$[\text{-P-O-Ni-O-P-}] + OH^- \rightarrow [\text{-P-O-Ni(OH)-O-P-}] + e^- \quad (6)$$

$$[\text{-P-O-Ni(OH)-O-P-}] + \text{glucose} \rightarrow \text{gluconolactone} + [\text{-P-O-Ni(OH)}_2\text{-O-P-}] \quad (7)$$

The deprotonation and isomerization of glucose is catalysed by the oxidative Ni^{3+} species in the electrode. This results the diffusion and removal of glucose intermediates/products into the bulk solution followed by the regeneration of active sites during the negative scan[58]. Fig. S8(c) shows the plot of scan rate normalized current density ($J_{pa}/\nu^{1/2}$) vs. scan rate (ν), where a polynomial decrease is observed, which indicates irreversible electrochemical catalytic (EC') process over the $Ni_3(PO_4)_2 \cdot 8H_2O$/NF catalyst surface[59]. The observed electrochemical catalytic (EC') mechanism of glucose oxidation was further supported by the Tafel plot (E_p vs. log I_p) shown in Fig. S8(d) and its inset, which has been derived from the rising part of the CV curve measured at 5 mV s^{-1} with 500 µM glucose. From the slope of Tafel region, the charge transfer coefficient was obtained using the relation:

$$Slope = \frac{(1-\alpha)nF}{2.303\,RT} \quad (8)$$

Here, α is charge transfer coefficient, n is number of electron in redox process (n= 2), F is Faraday constant (96485 C mol^{-1}), R is gas constant (8.314 J mol^{-1} K^{-1}) and T is the temperature (298 K). Based on the above mentioned quasi reversible electron transfer kinetics, the estimated charge transfer coefficient for electro-oxidation of glucose is 0.74 and indicates the two electron transfer process[60].

We further examined the electrocatalytic behavior of the 3D $Ni_3(PO_4)_2{\cdot}8H_2O$/NF towards different concentration of glucose. Fig. 6(a) shows the CV of $Ni_3(PO_4)_2{\cdot}8H_2O$/NF electrode where the current density for oxidation peak increases with increased glucose concentration from 10 µM to 2 mM. Noticeably, the cathodic peak current also increases significantly with the enhancement of glucose concentration, indicating the observed EC' process is different from characteristic catalytic oxidation in which the cathodic peak should decreases. Since the Ni^{2+} bound to the phosphate with oxygen atoms, there is the possibility of reorganization of bonds (breaking Ni-P bonds and generating new O-Ni-OH bonds) that could results electro-oxidation of glucose at a different kinetic rate[58]. Thereby, significant enhancement in cathodic peak current is observed along with the anodic peak current. Similar results were reported previously and the detailed explanations are presented in Supporting Information (SI) with more CV analysis in different concentration of NaOH solutions (Fig. S9 (a and b)). The corresponding derivative plot in Fig. 6(b) suggests that the anodic peak current density increases linearly with the rise of glucose concentration from 50 to 1,000 µM with a correlation coefficient, R^2 = 0.9892. The deviation at the high glucose concentration (>1000 µM) may be due to the passivation of the electrode and/or the glucose isomer. The measured slope at the linear range of the calibration curve gives a remarkable sensitivity of 24.39 $mAmM^{-1}cm^{-2}$ for the $Ni_3(PO_4)_2{\cdot}8H_2O$/NF based sensor. The limit of detection is evaluated from the linear regression curve using the relation 3σ/slope [61], where σ is the standard deviation of the blank NF and is around 97 nM (S/N=3) with a fast response time of less than 10 s. Table S2 in SI compare our $Ni_3(PO_4)_2{\cdot}8H_2O$/NF sensor with other non-enzymatic sensors for glucose detection. It can be clearly seen that our nickel phosphate based sensor showed state of the art

sensitivity. The $Ni_3(PO_4)_2 \cdot 8H_2O$/NF catalyst shows excellent linearity within a range of 50 - 1000 µM, which is comparable to other non-enzymatic glucose sensor. However, the limit of detection for the proposed sensor is limited to 1000 µM, while the actual blood glucose level is 4 – 7 mM and thereby needed to be improved further. Meantime, our sensor can be a better choice to validate the glucose level in sweat (10-1000 µM) and food products, which has low glucose concentration[19, 62-63].

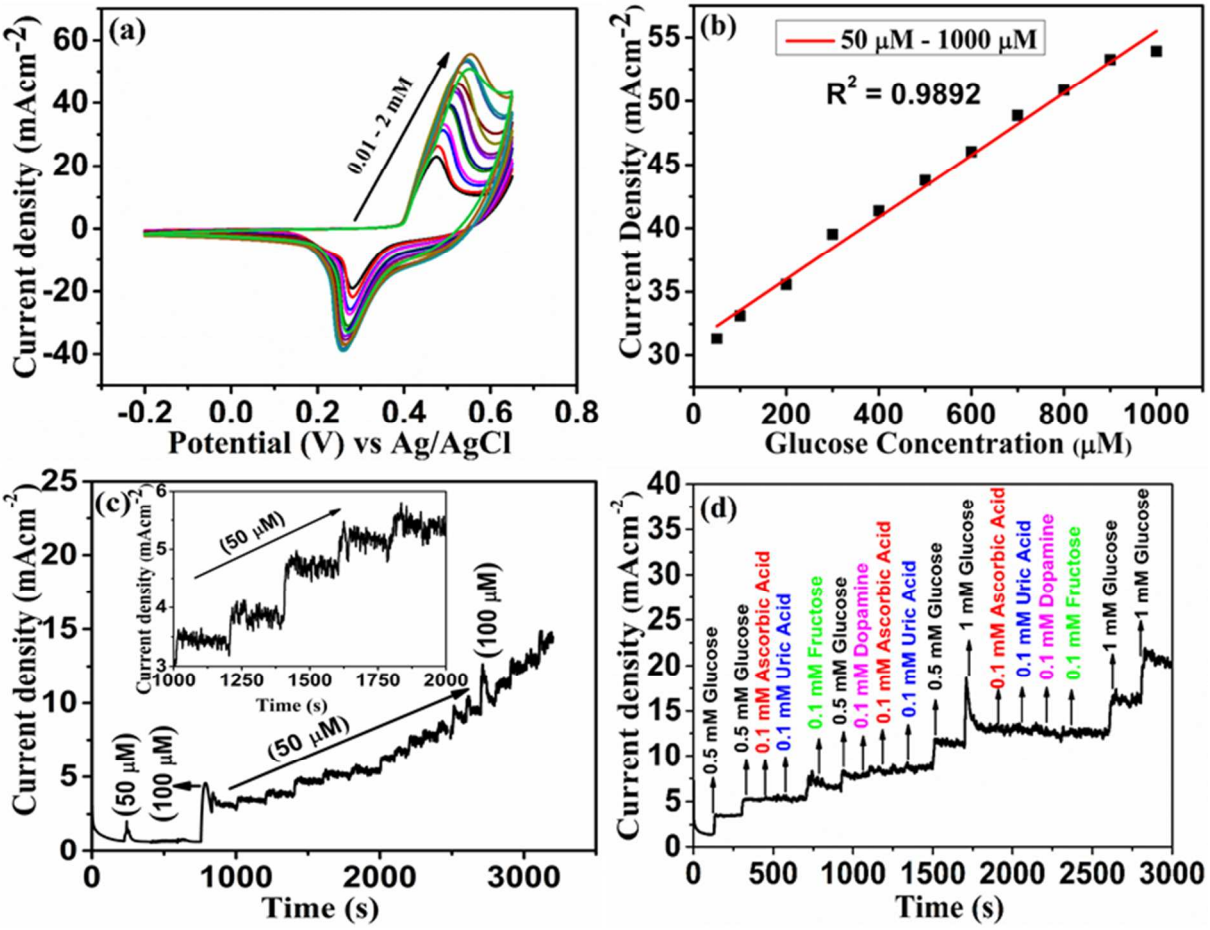

Figure 6. (a) CV curves measured at 5 mVs^{-1} at various glucose concentrations (10 µM to 2 mM), (b) The corresponding derivative plot, (c) Amperometric response of $Ni_3(PO_4)_2 \cdot 8H_2O$/NF catalyst at 0.45 V upon successive addition of 10 and 100 µM glucose, (d) Interference study showing Amperometric response of the electrode upon successive additions of 0.5 mM glucose, 100 µM ascorbic acid, 100 µM uric acid, 100 µM dopamine at 0.45 V vs. Ag/AgCl; background electrolyte 1M NaOH.

To understand more about the electro-oxidation of glucose and to estimate the catalytic rate constant, the chronoamperometric technique has been used. Fig. S10(a) shows the chronoamperometric measurements carried out in 1 M NaOH solutions containing various concentrations of glucose (0, 100, 500, 1000, 1500 and 2000 μM) at an applied potential of 0.45 V vs. Ag/AgCl. The exponential characteristic of (I-t) curve with increasing current with the glucose concentration further verifies the diffusion controlled electro-oxidation of glucose by [-P-O-Ni(OH)-O-P-] catalyst. Typical catalytic rate constant (K_{cat}) and diffusion coefficient (D) of glucose for $Ni_3(PO_4)_2{\cdot}8H_2O$/NF were estimated from the Cottrel relation. From the chronoamperometry (*I-t*) graph, the derivative plot between i_{cat}/i_L vs. $t^{1/2}$ shown in Fig. S10(b) was used to calculate the catalytic rate constant K_{cat}:[64-65]

$$\left(\frac{i_{cat}}{i_L}\right) = \pi^{1/2}(K_{cat}\ C\ t)^{1/2} \quad (9)$$

where, i_{cat} and i_L are the currents obtained in the *I-t* curve from $Ni_3(PO_4)_2{\cdot}8H_2O$/NF with and without 500 μM glucose in 1 M NaOH, respectively, C is the glucose concentration and t is time in seconds. From the slope of plot i_{cat}/i_L vs. $time^{1/2}$, the estimated K_{cat} for 500 μM glucose was 1.5×10^7 cm^3 M^{-1} s^{-1} and reveals good catalytic response of $Ni_3(PO_4)_2{\cdot}8H_2O$/NF surface for glucose detection. Meanwhile, *current* vs. $time^{-1/2}$ plot for different concentration of glucose has been drawn from the linear part of the *I-t* curve (Fig. S10a) and shown in Fig. S10(c). In order to evaluate the diffusion coefficient (D), the slopes of (*current* vs. $time^{-1/2}$) vs. Glucose concentration was plotted (Fig. S10d) and D is estimated from the following relation:[64-65]

$$i = \frac{nFAD^{1/2}C}{(\pi t)^{1/2}} \quad (10)$$

By using the slope of the line, the observed mean diffusion coefficient for glucose was found to be 4.8×10^{-9} cm^2 s^{-1}. Therefore, it can be concluded that diffusion-controlled process is dominated during the electro-oxidation of glucose.

Fig. 6(c) shows the amperometric response of the $Ni_3(PO)_4.8H_2O$/NF electrode at an applied voltage of 0.45 V upon successive addition of 50 or 100 µM glucose. For each addition of glucose, a significant current increment is observed (inset Fig. 6c), which indicates good catalytic activity of the electrode for continuous glucose monitoring. The observed high sensitivity and quick response time of the proposed non-enzymatic glucose sensor can be attributed to high surface to volume ratio of 3D nano/micro flake layered structure, which enhanced the electro-catalytic activity. In a practical use of non-enzymatic glucose sensor, specificity or selectivity is an important property that needs attention. It is reported that dopamine (DA), uric acid (UA), ascorbic acid (AA), and other carbohydrate compounds are the major co-existing oxidative elements with glucose in biological sample and consequently interfere with the detection of glucose. As shown in Fig. 6(d), the influence of these interfering species in detecting glucose is ≤3% for DA, and negligible for all the other elements, indicating superior selectivity of $Ni_3(PO_4)_2{\cdot}8H_2O$/NF based sensor. Since the isoelectric point for Ni is ~8.5 - 11, it would be negatively charged as similar to the negatively charged interference species due to the deprotonated effect in alkaline solution.[66] Thereby, both the negatively charged elements will repel each other and as a result should have negligible effect in the glucose detection. Furthermore, the long term stability of the sensor was investigated by measuring the CV at different time periods (Fig. S11). The output current density retained ~96.6% of its initial value after 30 days confirming excellent stability of the $Ni_3(PO_4)_2{\cdot}8H_2O$/NF electrode for long term applications. This high stability of the electrode is mainly due to the strong adhesion of $Ni_3(PO_4)_2{\cdot}8H_2O$/NF nano/micro flake layers on nickel foam, originating from its direct integration and structural stability in NaOH base solution.

Sweat based pH sensor studies

Metal oxide based pH sensors can be a viable alternative to commercial glass pH sensors. Here, for the first time we are proposing $Ni_3(PO_4)_2{\cdot}8H_2O$ nano/micro flakes electrode for pH sensing in human sweat.

In general, the pH is a measure of H^+ ion concentration in a solution. Further, it can be explained using Nernest equation [67], which shows the direct proportionality of solution pH against the measured potential difference between reference and working electrode. The electrode pH response was initially investigated in Britton-Robinson (B-R) buffer solution as shown in Fig. 7(a-c). By changing the pH value, the corresponding equilibrium potential has been measured (Fig. 7a). The potential equilibrium response time is around 115 s for the pH value 2 - 7. The linear regression of the potentiometric responses as a function of the pH values (2 - 7) is shown in Fig. 7(b), where the correlation coefficients is 0.97. Fig. 7(c) shows the open circuit potential as a function of subsequent change in pH. The sensitivity of the electrode is about 34.18 mV/pH, which is ~58% of Nernst response (59.2 mV/pH)[67]. The exact reaction mechanism of pH responsive metal oxide catalyst in the solution is still not clearly understood. Since, crystalline water is present in the catalyst, the reaction mechanism are more complicated than the metal oxide electrodes. Under aqueous exposure, the catalyst surface could be charged due to the reactions of H^+/OH^- ions. With the solution pH, the charged hydroxyl groups either able to donate or accept proton from the solution[68]. In case of $Ni_3(PO_4)_2{\cdot}8H_2O$/NF electrode, the presence of hydrated phase actively involves into protonation and deprotonation reaction and thereby reasonable Nernst pH response was observed. Further surface modification is needed to enhance the pH sensitivity up to actual Nernst response. However, it should be noted that the pH sensing capability of our catalyst is limited to 2-7, since the catalyst surface starts to hydrolyze at high pH and readily oxygen evolution occurs[69]. Thus results in the dissolution of catalyst within the electrolyte beyond pH 7. Interestingly, the observed pH range (2-7) of our sensor encompass the physiological range of human sweat (4-7), and thereby it can be concluded that the proposed $Ni_3(PO_4)_2{\cdot}8H_2O$/NF catalyst could be a suitable candidate for sweat based pH sensor.

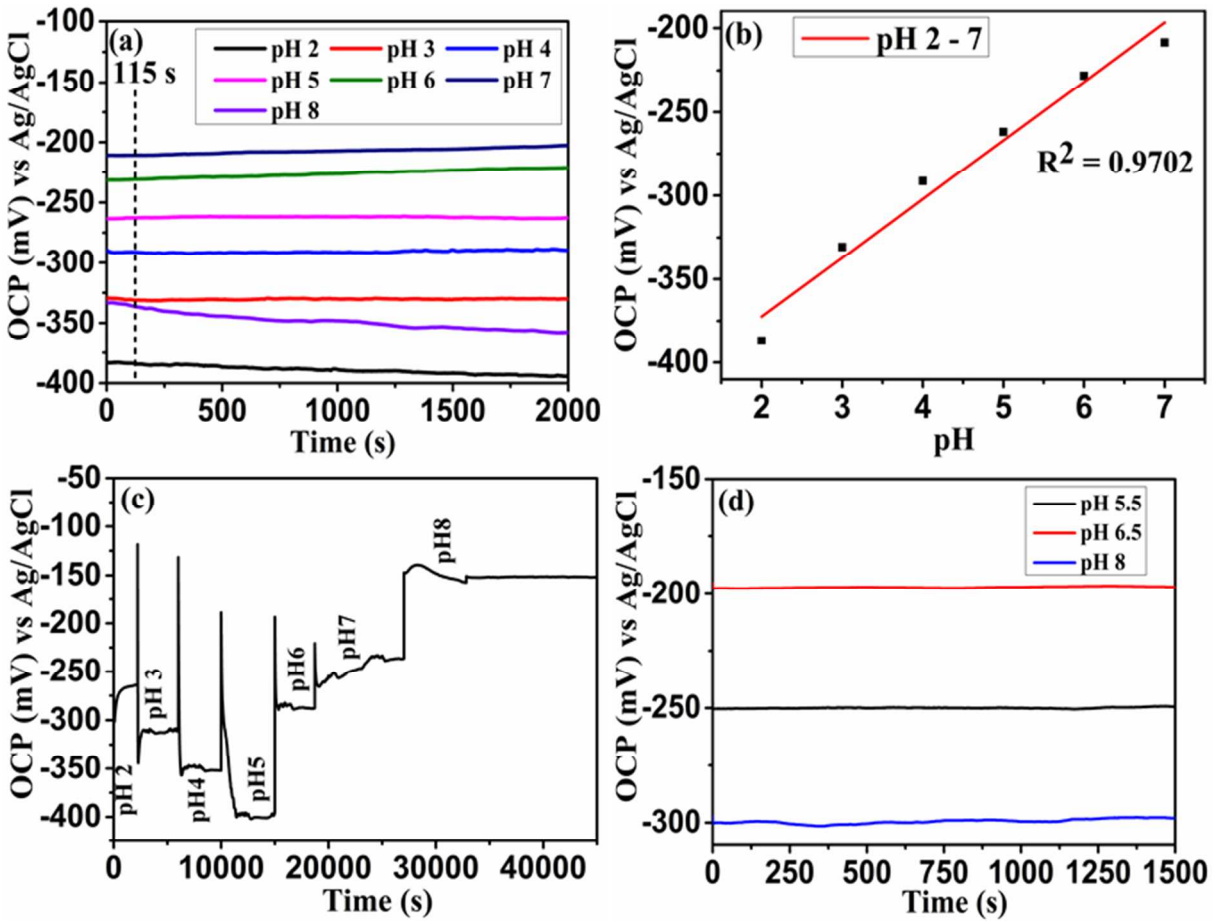

Figure 7. (a) Potential response of $Ni_3(PO_4)_2{\cdot}8H_2O$/NF catalyst at different pH (2-8) in buffer-solution and (b) the corresponding linear relation plot, (c) Potential response curve for subsequent variation of pH from 2 to 8 and (d) Typical potential variation of $Ni_3(PO_4)_2{\cdot}8H_2O$/NF in stimulated sweat at various pH values.

The proposed $Ni_3(PO_4)_2{\cdot}8H_2O$/NF electrode was applied to determine the pH of stimulated sweat samples having three different standard pH values of 5.5, 6.5 and 8 (Fig. 7d). It can be seen that the potential response (49 mV/pH) is relatively good and comparable with Nernst response at low pH values (5.5 and 6.5), which are the most common pH of healthy human body.[70] For practical application, the sensing performance of pH sensor should not be influenced by other ions present in sweat. The main components of sweat and their concentrations are given in Table S3 of the SI. Fig. S12 shows the interference study of the catalyst by varying the pH (2-8), which further exposes good tolerance against

the interferences. Therefore, it can be concluded that $Ni_3(PO_4)_2 \cdot 8H_2O$/NF catalyst could be an excellent choice for sweat (pH 4-7) based electrochemical sensor due to its good sensitivity, quick response time and excellent selectivity for reliable detection of pH of human sweat.

Conclusions

In summary, 3D nano/micro flakes of $Ni_3(PO_4)_2 \cdot 8H_2O$/NF on nickel foam (NF) is developed using a simple hydrothermal approach. $Ni_3(PO_4)_2 \cdot 8H_2O$/NF shows a superior electrochemical performance as a supercapattery electrode, which delivers a specific capacity of 301.8 mAh g^{-1} at a specific current of 5 mA cm^{-2}. The fabricated supercapattery based on the $Ni_3(PO_4)_2 \cdot 8H_2O$/NF and AC/NF as the positive and negative electrodes showed an specific energy and power of 33.4 Wh kg^{-1} and 165.5 W kg^{-1} with impressive cyclic stability of 89% after 10,000 cycles. At the same time, the proposed electrode has been successfully applied as a non-enzymatic glucose sensor. The sensor has a high sensitivity, low detection limit and excellent selectivity. Furthermore, as an alternative to the commercial glass pH electrode, the same material was evaluated for sweat based pH sensor. The potentiometric response of this sensor is appreciably linear to a pH range from 2 to 7. Thereby, we have developed a multifunctional sensor for the detection of glucose and pH simultaneously. This work provides a new platform in the novel material design philosophy for transition metal phosphates, especially for potential applications in electrochemical energy storage as well as bi-functional electrocatalysts for glucose and pH sensing.

ACKNOWLEDGMENT

The authors acknowledge the financial support from Science Foundation Ireland under the Technology Innovation and Development Award no. 14/TIDA/2455. We acknowledge support from EU FP7 project MANpower (contract number: 604360).

SUPPORTING INFORMATION

The FTIR and EDS spectrum of $Ni_3(PO_4)_2{\cdot}8H_2O$/NF nano/micro flakes, N_2 absorption and desorption isotherm and their pore size distribution (inset) of $Ni_3(PO_4)_2{\cdot}8H_2O$, CV curves of sample AC/NF and $Ni_3(PO_4)_2{\cdot}8H_2O$/NF in 1M NaOH solution at 10 mV s^{-1}, Nyquist plot of $Ni_3(PO)_4{\cdot}8H_2O$ /NF ||AC/NF supercapattery before and after 10000 charge-discharge cycles, CV curves of pure NF, $Ni_3(PO_4)_2{\cdot}8H_2O$/NF absence and presence of (500 μM) glucose at 5 mV s^{-1} in 1 M NaOH, CV of nickel phosphate catalyst at various scan rate in 1 M NaOH with 500 μM glucose and the corresponding linear regression for both anodic and cathodic current response, the plots of log I_{pa} vs. log ν, $J_{pa}/\nu^{1/2}$ vs. ν and steady state current-voltage curve of $Ni_3(PO_4)_2{\cdot}8H_2O$/NF catalyst in 1 M NaOH with 500 μM glucose at 5 mV s^{-1}, Chronoamperograms of $Ni_3(PO_4)_2{\cdot}8H_2O$/NF catalyst in the absence and presence of glucose at different concentrations and their derivative plots, Current response of $Ni_3(PO_4)_2{\cdot}8H_2O$ /NF glucose sensor measured at different time periods, Interference studies of $Ni_3(PO_4)_2{\cdot}8H_2O$ based pH sensor. Table S1, Table S2 and Table S3 represents the comparison of electrochemical energy storage, glucose detection and human sweat composition respectively. The Supporting Information is available free of charge on the ACS Publications website at http://pubs.acs.org.

References

1. Kakooei, S.; Ismail, M. C.; Ari-Wahjoedi, B., An Overview of pH Sensors Based on Iridium Oxide: Fabrication and Application. *Int. J. Mater. Sci. Innovat* **2013,** *1*, 62-72.
2. Wang, J., Electrochemical Glucose Biosensors. *Chem. Rev.* **2008,** *108* (2), 814-825.
3. Winter, M.; Brodd, R. J., What are Batteries, Fuel Cells, and Supercapacitors? *Chem. Rev.* **2004,** *104* (10), 4245-4269.
4. Jung, S.; Lee, J.; Hyeon, T.; Lee, M.; Kim, D. H., Fabric-Based Integrated Energy Devices for Wearable Activity Monitors. *Adv. Mater.* **2014,** *26* (36), 6329-6334.
5. Zhong, J.; Zhang, Y.; Zhong, Q.; Hu, Q.; Hu, B.; Wang, Z. L.; Zhou, J., Fiber-Based Generator for Wearable Electronics and Mobile Medication. *ACS nano* **2014,** *8* (6), 6273-6280.
6. Simon, P.; Gogotsi, Y., Materials for Electrochemical Capacitors. *Nat. Mater.* **2008,** *7* (11), 845-854.
7. Miller, J. R.; Simon, P., Electrochemical Capacitors for Energy Management. *Science* **2008,** *321* (5889), 651-652.
8. Scognamiglio, V., Nanotechnology in Glucose Monitoring: Advances and Challenges in the Last 10 Years. *Biosens. Bioelectron.* **2013,** *47*, 12-25.

9. Yu, Z.; Tetard, L.; Zhai, L.; Thomas, J., Supercapacitor Electrode Materials: Nanostructures from 0 to 3 Dimensions. *Energy Environ. Sci.* **2015,** *8* (3), 702-730.
10. Choi, W.; Choudhary, N.; Han, G. H.; Park, J.; Akinwande, D.; Lee, Y. H., Recent Development of Two-Dimensional Transition Metal Dichalcogenides and their Applications. *Mater. Today* **2017,** *20* (3), 116-130.
11. Li, X.; Elshahawy, A. M.; Guan, C.; Wang, J., Metal Phosphides and Phosphates-Based Electrodes for Electrochemical Supercapacitors. *Small* **2017,** *13* (39), 1701530.
12. Yang, C.; Dong, L.; Chen, Z.; Lu, H., High-Performance all-Solid-State Supercapacitor Based on the Assembly of Graphene and Manganese(II) Phosphate Nanosheets. *J. Phys. Chem. C* **2014,** *118* (33), 18884-18891.
13. Wang, S.; Pang, H.; Zhao, S.; Shao, W.; Zhang, N.; Zhang, J.; Chen, J.; Li, S., $NH_4CoPO_4{\cdot}H_2O$ Microbundles Consisting of One-Dimensional Layered Microrods for High Performance Supercapacitors. *RSC Adv.* **2014,** *4* (1), 340-347.
14. Liu, M.-C.; Li, J.-J.; Hu, Y.-X.; Yang, Q.-Q.; Kang, L., Design and Fabrication of $Ni_3P_2O_8$-$Co_3P_2O_8{\cdot}8H_2O$ as Advanced Positive Electrodes for Asymmetric Supercapacitors. *Electrochim. Acta* **2016,** *201*, 142-150.
15. Chae, J. H.; Zhou, X.; Chen, G. Z., From Electrochemical Capacitors to Supercapatteries. *Green* **2012,** *2* (1), 41-54.
16. Toghill, K. E.; Compton, R. G., Electrochemical Non-Enzymatic Glucose Sensors: A Perspective and an Evaluation. *Int. J. Electrochem. Sci* **2010,** *5* (9), 1246-1301.
17. Zhu, H.; Li, L.; Zhou, W.; Shao, Z.; Chen, X., Advances in Non-Enzymatic Glucose Sensors Based on Metal Oxides. *J. Mater. Chem. B* **2016,** *4* (46), 7333-7349.
18. Huang, W.-D.; Cao, H.; Deb, S.; Chiao, M.; Chiao, J.-C., A Flexible pH Sensor Based on the Iridium Oxide Sensing Film. *Sens. Actuators, A : Physical* **2011,** *169* (1), 1-11.
19. Lee, H.; Song, C.; Hong, Y. S.; Kim, M. S.; Cho, H. R.; Kang, T.; Shin, K.; Choi, S. H.; Hyeon, T.; Kim, D.-H., Wearable/Disposable Sweat-Based Glucose Monitoring Device with Multistage Transdermal Drug Delivery Module. *Sci. Adv.* **2017,** *3* (3), e1601314.
20. Natan, M. J.; Belanger, D.; Carpenter, M. K.; Wrighton, M. S., pH-Sensitive Nickel (II) Hydroxide-Based Microelectrochemical Transistors. *J. Phys. Chem.* **1987,** *91* (7), 1834-1842.
21. Zaman, S.; Asif, M.; Zainelabdin, A.; Amin, G.; Nur, O.; Willander, M., CuO Nanoflowers as an Electrochemical pH Sensor and the Effect of pH on the Growth. *J. Electroanal. Chem.* **2011,** *662* (2), 421-425.
22. Zhang, Q.; Liu, W.; Sun, C.; Zhang, H.; Pang, W.; Zhang, D.; Duan, X., On-Chip Surface Modified Nanostructured Zno as Functional pH Sensors. *Nanotechnology* **2015,** *26* (35), 355202.
23. Zhang, J.; Yang, Y.; Zhang, Z.; Xu, X.; Wang, X., Rapid Synthesis of Mesoporous $Ni_xCo_{3-x}(PO_4)_2$ Hollow Shells Showing Enhanced Electrocatalytic and Supercapacitor Performance. *J. Mater. Chem. A* **2014,** *2* (47), 20182-20188.
24. Zhao, Y.; Chen, Z.; Xiong, D.-B.; Qiao, Y.; Tang, Y.; Gao, F., Hybridized Phosphate with Ultrathin Nanoslices and Single Crystal Microplatelets for High Performance Supercapacitors. *Sci. Rep.* **2016,** *6* 17613.
25. Pang, H.; Yan, Z.; Wang, W.; Chen, J.; Zhang, J.; Zheng, H., Facile Fabrication of $NH_4CoPO_4{\cdot}H_2O$ Nano/Microstructures and Their Primarily Application as Electrochemical Supercapacitor. *Nanoscale* **2012,** *4* (19), 5946-5953.
26. Shao, H.; Padmanathan, N.; McNulty, D.; O' Dwyer, C.; Razeeb, K. M., Supercapattery Based on Binder-Free $Co_3(PO_4)_2{\cdot}8H_2O$ Multilayer Nano/Microflakes on Nickel Foam. *ACS Appl. Mater. Interfaces* **2016,** *8* (42), 28592-28598.

27. Gerken, J. B.; McAlpin, J. G.; Chen, J. Y.; Rigsby, M. L.; Casey, W. H.; Britt, R. D.; Stahl, S. S., Electrochemical Water Oxidation with Cobalt-Based Electrocatalysts from pH 0–14: the Thermodynamic Basis for Catalyst Structure, Stability, and Activity. *J. Amer. Chem. Soc.* **2011,** *133* (36), 14431-14442.
28. Risch, M.; Grimaud, A.; May, K. J.; Stoerzinger, K. A.; Chen, T. J.; Mansour, A. N.; Shao-Horn, Y., Structural Changes of Cobalt-Based Perovskites Upon Water Oxidation Investigated by EXAFS. *J. Phys. Chem. C* **2013,** *117* (17), 8628-8635.
29. Allen, M. J.; Myer, B. J.; Millett, P. J.; Rushton, N., The Effects of Particulate Cobalt, Chromium and Cobalt-Chromium Alloy on Human Osteoblast-Like Cells In-Vitro. *J Bone Joint Surg. Br.* **1997,** *79* (3), 475-482.
30. Zhao, J.; Pang, H.; Deng, J.; Ma, Y.; Yan, B.; Li, X.; Li, S.; Chen, J.; Wang, W., Mesoporous Uniform Ammonium Nickel Phosphate Hydrate Nanostructures as High Performance Electrode Materials for Supercapacitors. *Cryst.Eng.Comm.* **2013,** *15* (30), 5950-5955.
31. Chen, T.; Liu, D.; Lu, W.; Wang, K.; Du, G.; Asiri, A. M.; Sun, X., Three-Dimensional Ni_2P Nanoarray: an Efficient Catalyst Electrode for Sensitive and Selective Nonenzymatic Glucose Sensing with High Specificity. *Anal. Chem.* **2016,** *88* (16), 7885-7889.
32. Hassaninejad-Darzi, S. K.; Gholami-Esfidvajani, M., Preparation Of Nanoporous Nickel Phosphate VSB-5 Nanorods Carbon Paste Electrode as Glucose Non-Enzymatic Sensor. *J Porous Mat.* **2017,** *24* (1), 85-95.
33. Kullyakool, S.; Danvirutai, C.; Siriwong, K.; Noisong, P., Determination of Kinetic Triplet of the Synthesized $Ni_3(PO_4)_2{\cdot}8H_2O$ by Non-Isothermal and Isothermal Kinetic Methods. *J. Therm. Anal. Calorim.* **2014,** *115* (2), 1497-1507.
34. Baril, M.; Assaaoudi, H.; Butler, I. S., Pressure-Tuning Raman Microspectroscopic Study of Cobalt (II), Manganese (II), Zinc (II) and Magnesium (II) Pyrophosphate Dihydrates. *J. Mol. Struct.* **2005,** *751* (1), 168-171.
35. Bontchev, R. P.; Iliev, M. N.; Dezaneti, L. M.; Jacobson, A. J., Two New Open Framework Cobalt Phosphates: $Naco_3(OH)(PO_4)_2.1/4H_2O$ and $Na(NH_4)Co_2(PO_4)_2.H_2O$. *Solid State Sci.* **2001,** *3* (1), 133-142.
36. Breitinger, D.; Belz, H.-H.; Hajba, L.; Komlósi, V.; Mink, J.; Brehm, G.; Colognesi, D.; Parker, S.; Schwab, R., Combined Vibrational Spectra of Natural Wardite. *J. Mol. Struct.* **2004,** *706* (1), 95-99.
37. Chapman, A.; Thirlwell, L., Spectra of Phosphorus Compounds—I The Infra-Red Spectra of Orthophosphates. *Spectrochim. Acta* **1964,** *20* (6), 937-947.
38. Preston, C. M.; Adams, W., A Laser Raman Spectroscopic Study of Aqueous Orthophosphate Salts. *J. Phys. Chem.* **1979,** *83* (7), 814-821.
39. Viswanathan, K.; Nayar, V.; Aruldhas, G., Infrared and Raman Spectra of Three Tetrametaphosphates $M_2P_4O_{12}$ (M=Fe, Ni, Zn). *J. Chem. Sci.* **1985,** *95* (5), 463-469.
40. Padmanathan, N.; Shao, H.; McNulty, D.; O'Dwyer, C.; Razeeb, K. M., Hierarchical NiO–In_2O_3 Microflower (3D)/Nanorod (1D) Hetero-Architecture as a Supercapattery Electrode with Excellent Cyclic Stability. *J. Mater. Chem. A* **2016,** *4* (13), 4820-4830.
41. Yu, M.; Wang, W.; Li, C.; Zhai, T.; Lu, X.; Tong, Y., Scalable Self-Growth of Ni@Nio Core-Shell Electrode with Ultrahigh Capacitance and Super-Long Cyclic Stability for Supercapacitors. *NPG Asia Mater.* **2014,** *6*, e129.
42. Senthilkumar, V.; Kadumudi, F. B.; Ho, N. T.; Kim, J.-W.; Park, S.; Bae, J.-S.; Choi, W. M.; Cho, S.; Kim, Y. S., NiO Nanoarrays of a Few Atoms Thickness on 3D Nickel Network for Enhanced Pseudocapacitive Electrode Applications. *J. Power Sources* **2016,** *303*, 363-371.
43. Sathiya, M.; Ramesha, K.; Rousse, G.; Foix, D.; Gonbeau, D.; Guruprakash, K.; Prakash, A. S.; Doublet, M. L.; Tarascon, J. M., Li_4NiTeO_6 as a Positive Electrode for Li-Ion Batteries. *Chem. Commun.* **2013,** *49* (97), 11376-11378.
44. Barr, T. L., Recent Advances in X-ray Photoelectron Spectroscopy Studies of Oxides. *J. Vac. Sci. Technol. A: Vacuum, Surfaces, and Films* **1991,** *9* (3), 1793-1805.

45. Zhao, B.; Ke, X.-K.; Bao, J.-H.; Wang, C.-L.; Dong, L.; Chen, Y.-W.; Chen, H.-L., Synthesis of Flower-Like NiO and Effects of Morphology on its Catalytic Properties. *J Phys. Chem. C* **2009,** *113* (32), 14440-14447.
46. Chen, G. Z., Supercapacitor and Supercapattery as Emerging Electrochemical Energy Stores. *Int. Mater. Rev.* **2017,** *62* (4), 173-202.
47. Bajdich, M.; García-Mota, M.; Vojvodic, A.; Nørskov, J. K.; Bell, A. T., Theoretical Investigation of the Activity of Cobalt Oxides for the Electrochemical Oxidation of Water. *J. Amer. Chem. Soc.* **2013,** *135* (36), 13521-13530.
48. Wu, G.; Li, N.; Zhou, D.-R.; Mitsuo, K.; Xu, B.-Q., Anodically Electrodeposited Co+Ni Mixed Oxide Electrode: Preparation and Electrocatalytic Activity for Oxygen Evolution in Alkaline Media. *J. Solid State Chem.* **2004,** *177* (10), 3682-3692.
49. Ding, J.; Wang, H.; Li, Z.; Cui, K.; Karpuzov, D.; Tan, X.; Kohandehghan, A.; Mitlin, D., Peanut Shell Hybrid Sodium Ion Capacitor with Extreme Energy–Power Rivals Lithium Ion Capacitors. *Energy Environ. Sci.* **2015,** *8* (3), 941-955.
50. Chen, C.; Zhang, N.; Liu, X.; He, Y.; Wan, H.; Liang, B.; Ma, R.; Pan, A.; Roy, V. A., Polypyrrole-Modified $NH_4NiPO_4{\cdot}H_2O$ Nanoplate Arrays on Ni Foam for Efficient Electrode in Electrochemical Capacitors. *ACS Sustainable Chem. Eng.* **2016,** *4* (10), 5578-5584.
51. Li, Q.; Li, Y.; Peng, H.; Cui, X.; Zhou, M.; Feng, K.; Xiao, P., Layered $NH_4Co_xNi_{1-x}PO_4{\cdot}H_2O$ ($0 \leqq x \leqq 1$) Nanostructures Finely Tuned by Co/Ni Molar Ratios for Asymmetric Supercapacitor Electrodes. *J Mater. Sci.* **2016,** *51* (22), 9946-9957.
52. Zhao, J.; Wang, S.; Run, Z.; Zhang, G.; Du, W.; Pang, H., Hydrothermal Synthesis of Nickel Phosphate Nanorods for High-Performance Flexible Asymmetric All-Solid-State Supercapacitors. *Part. Part. Syst. Char.* **2015,** *32* (9), 880-885.
53. Ho, J.; Tremiliosi Filho, G.; Simpraga, R.; Conway, B., Structure Influence on Electrocatalysis and Adsorption of Intermediates in the Anodic O_2 Evolution at Dimorphic α-and β-PbO_2. *J. Electroanal. Chem.* **1994,** *366* (1-2), 147-162.
54. Rodbard, D., Continuous Glucose Monitoring: A Review of Successes, Challenges, and Opportunities. *Diabetes Technol. Ther.* **2016,** *18* (S2), S2-3-S2-13.
55. Cengiz, E.; Sherr, J. L.; Weinzimer, S. A.; Tamborlane, W. V., New-Generation Diabetes Management: Glucose Sensor-Augmented Insulin Pump Therapy. *Expert Rev. Med. Devices* **2011,** *8* (4), 449-458.
56. Hassaninejad-Darzi, S. K., Fabrication of a Non-Enzymatic Ni(ii) Loaded ZSM-5 Nanozeolite and Multi-Walled Carbon Nanotubes Paste Electrode as a Glucose Electrochemical Sensor. *RSC Adv.* **2015,** *5* (128), 105707-105718.
57. Li, G.; Wang, X.; Liu, L.; Liu, R.; Shen, F.; Cui, Z.; Chen, W.; Zhang, T., Controllable Synthesis of 3D $Ni(OH)_2$ and NiO Nanowalls on Various Substrates for High-Performance Nanosensors. *Small* **2015,** *11* (6), 731-739.
58. Martín-Yerga, D.; Carrasco-Rodríguez, J.; Fierro, J. L. G.; García Alonso, F. J.; Costa-García, A., Copper-Modified Titanium Phosphate Nanoparticles as Electrocatalyst for Glucose Detection. *Electrochim. Acta* **2017,** *229*, 102-111.
59. Vaidyanathan, S.; Cherng, J.-Y.; Sun, A.-C.; Chen, C.-Y., Bacteria-Templated NiO Nanoparticles/Microstructure for an Enzymeless Glucose Sensor. *Int. J. Mol. Sci.* **2016,** *17* (7), 1104.
60. Beitollah, H.; Goodarzian, M.; Khalilzadeh, M. A.; Karimi-Maleh, H.; Hassanzadeh, M.; Tajbakhsh, M., Electrochemical Behaviors and Determination of Carbidopa on Carbon Nanotubes Ionic Liquid Paste Electrode. *J Mol Liq.* **2012,** *173*, 137-143.
61. Kumary, V. A.; Nancy, T. M.; Divya, J.; Sreevalsan, K., Nonenzymatic Glucose Sensor: Glassy Carbon Electrode Modified with Graphene-Nickel/Nickel Oxide Composite. *Int. J. Electrochem. Sci* **2013,** *8*, 2220-2228.

62. Moyer, J.; Wilson, D.; Finkelshtein, I.; Wong, B.; Potts, R., Correlation Between Sweat Glucose and Blood Glucose in Subjects with Diabetes. *Diabetes Technol. Ther.* **2012,** *14* (5), 398-402.
63. Sakaguchi, K.; Hirota, Y.; Hashimoto, N.; Ogawa, W.; Hamaguchi, T.; Matsuo, T.; Miyagawa, J.-I.; Namba, M.; Sato, T.; Okada, S., Evaluation of a Minimally Invasive System for Measuring Glucose Area Under the Curve During Oral Glucose Tolerance Tests: Usefulness of Sweat Monitoring for Precise Measurement. *J Diabetes Sci. Technol.* **2013,** *7* (3), 678-688.
64. Kanyong, P.; Rawlinson, S.; Davis, J., Fabrication and Electrochemical Characterization of Polydopamine Redox Polymer Modified Screen-Printed Carbon Electrode for the Detection of Guanine. *Sens. Actuators, B: Chemical* **2016,** *233*, 528-534.
65. Sattarahmady, N.; Heli, H., A Non-Enzymatic Amperometric Sensor for Glucose Based on Cobalt Oxide Nanoparticles. *J. Exp. Nanosci.* **2012,** *7* (5), 529-546.
66. Mahmood, T.; Saddique, M. T.; Naeem, A.; Westerhoff, P.; Mustafa, S.; Alum, A., Comparison of Different Methods for the Point of Zero Charge Determination of NiO. *Ind. Eng. Chem. Res.* **2011,** *50* (17), 10017-10023.
67. Manjakkal, L.; Cvejin, K.; Kulawik, J.; Zaraska, K.; Szwagierczak, D.; Socha, R. P., Fabrication of Thick Film Sensitive RuO_2-TiO_2 And Ag/AgCl/KCl Reference Electrodes and their Application for pH Measurements. *Sens. Actuators, B: Chemical* **2014,** *204*, 57-67.
68. Tombácz, E., pH-Dependent Surface Charging of Metal Oxides. *Period. Polytech., Chem. Eng.* **2009,** *53* (2), 77.
69. Kurzweil, P., Metal Oxides and Ion-Exchanging Surfaces as pH Sensors in Liquids: State-of-the-Art and Outlook. *Sensors* **2009,** *9* (6), 4955-4985.
70. Jadoon, S.; Karim, S.; Akram, M. R.; Kalsoom Khan, A.; Zia, M. A.; Siddiqi, A. R.; Murtaza, G., Recent Developments in Sweat Analysis and Its Applications. *Int J Anal Chem.* **2015,** *2015,* 164974(7 pages).

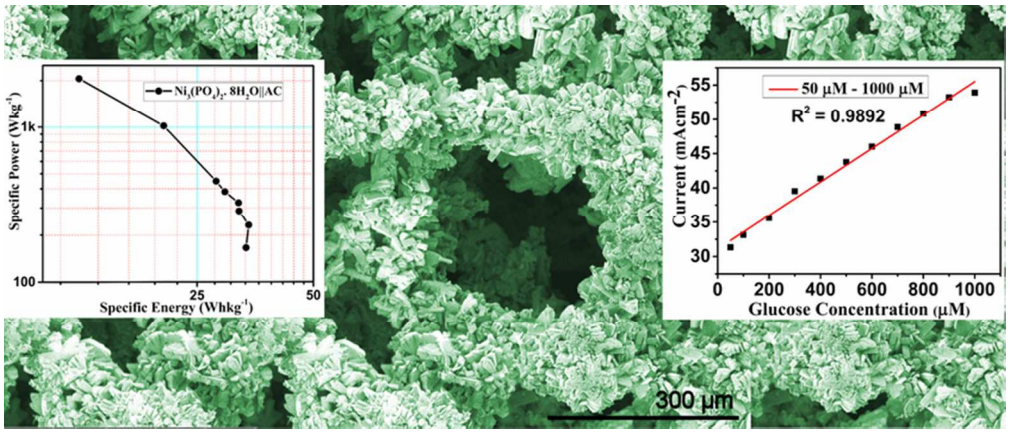

Table of Contents Graphic

35x15mm (600 x 600 DPI)